



Development of TiNbTaZrMo bio-high entropy alloy (BioHEA) super-solid solution by selective laser melting, and its improved mechanical property and biocompatibility

Takuya Ishimoto^{a,b}, Ryosuke Ozasa^{a,b}, Kana Nakano^a, Markus Weinmann^c, Christoph Schnitter^c, Melanie Stenzel^c, Aira Matsugaki^a, Takeshi Nagase^{a,d}, Tadaaki Matsuzaka^a, Mitsuharu Todai^e, Hyoung Seop Kim^f, Takayoshi Nakano^{a,b,*}

^a Division of Materials and Manufacturing Science, Graduate School of Engineering, Osaka University, 2-1 Yamadaoka, Suita, Osaka 565-0871, Japan

^b Anisotropic Design & Additive Manufacturing Research Center, Osaka University, 2-1 Yamadaoka, Suita, Osaka 565-0871, Japan

^c TANIOBIS GmbH, 78-91 Im Schleeke, Goslar D-38642, Germany

^d Research Center for Ultra-High Voltage Electron Microscopy, Osaka University, 7-1 Mihogaoka, Ibaraki, Osaka 567-0047, Japan

^e Department of Environmental Materials Engineering, National Institute of Technology, Niihama College, 7-1 Yagumo-cho Niihama, Ehime 792-8580, Japan

^f Department of Materials Science and Engineering, Pohang University of Science and Technology, Pohang 37673, South Korea

ARTICLE INFO

Article history:

Received 11 November 2020

Revised 2 December 2020

Accepted 2 December 2020

Keywords:

Selective laser melting

High entropy alloy

BioHEA

Cooling rate

Segregation suppression

ABSTRACT

BioHEAs, specifically designed high entropy alloy (HEA) systems for biomedical applications, represent a new era for biomaterials. However, recent challenges are (1) the poor shape customizability, and (2) the inevitable severe segregation due to the intrinsic fact that HEA is an ultra-multicomponent alloy system. To achieve shape customization and suppression of elemental segregation simultaneously, we used an extremely high cooling rate ($\sim 10^7$ K/s) of the selective laser melting (SLM) process. We, for the first time, developed pre-alloyed $\text{Ti}_{1.4}\text{Nb}_{0.6}\text{Ta}_{0.6}\text{Zr}_{1.4}\text{Mo}_{0.6}$ BioHEA powders and SLM-built parts with low porosity, customizable shape, excellent yield stress, and good biocompatibility. The SLM-built specimens showed drastically suppressed elemental segregation compared to the cast counterpart, representing realization of a super-solid solution. As a result, the 0.2% proof stress reached 1690 ± 78 MPa, which is significantly higher than that of cast $\text{Ti}_{1.4}\text{Nb}_{0.6}\text{Ta}_{0.6}\text{Zr}_{1.4}\text{Mo}_{0.6}$ (1140 MPa). The SLM-built $\text{Ti}_{1.4}\text{Nb}_{0.6}\text{Ta}_{0.6}\text{Zr}_{1.4}\text{Mo}_{0.6}$ BioHEA is promising as a next-generation metallic material for biomedical applications.

© 2020 Acta Materialia Inc. Published by Elsevier Ltd.

This is an open access article under the CC BY license (<http://creativecommons.org/licenses/by/4.0/>)

Manuscript

It is highly desirable that next-generation metallic biomaterials for orthopedic and dental implants exhibit superior mechanical performance and biocompatibility and shape customizability to fit individual patients' skeletons [1]. In this study, to the best of our knowledge, we first attempted to create such excellent metallic biomaterials using an approach that combines a state-of-the-art material and manufacturing technology—a high-entropy alloy (HEA) for biomedical applications, called BioHEA, and selective laser melting (SLM) as a powder bed fusion-type additive manufacturing (AM) method.

BioHEAs are specifically designed HEAs, composed of non-biotoxic elements. For the first time, our group proposed a novel equiatomic Ti–Nb–Ta–Zr–Mo HEA and demonstrated its potential as a new class of metallic biomaterials owing to its excellent mechanical properties and biocompatibility compared to those of pure Ti [2]. We then optimized the composition and developed new alloy systems, resulting in $\text{Ti}_{2.6}\text{NbTaZrMo}$, $\text{Ti}_{1.7}\text{NbTaZrMo}_{0.5}$, $\text{Ti}_{1.5}\text{NbTaZrMo}_{0.5}$, $\text{Ti}_{1.4}\text{Nb}_{0.6}\text{Ta}_{0.6}\text{Zr}_{1.4}\text{Mo}_{0.6}$ [3–5], $\text{TiZrHfCr}_{0.2}\text{Mo}$, and $\text{TiZrHfCo}_{0.07}\text{Cr}_{0.07}\text{Mo}$ [6] with excellent biocompatibility. Many researchers have developed new BioHEAs [7–9], and characterized their properties [7–11]. Research interest in BioHEAs is now growing rapidly, and the issue to be overcome has been identified as the improvement of the integrity of BioHEAs. One reason behind this drawback is the poor shape customizability and another is the remarkably high segregation tendency during solidification [2,4,5,12,13]. Because HEAs are ultra-multicomponent alloy systems, elemental segregation is highly likely. Extensive elemental

* Corresponding author at: Division of Materials and Manufacturing Science, Graduate School of Engineering, Osaka University, 2-1 Yamadaoka, Suita, Osaka 565-0871, Japan.

E-mail address: nakano@mat.eng.osaka-u.ac.jp (T. Nakano).

segregation would lead to a heterogeneous elemental distribution that could reduce sophisticated properties peculiar to BioHEAs.

SLM is a suitable method for simultaneously achieving shape customization and suppressing segregation during solidification. Regarding elemental segregation during solidification, the cooling rate is considered to be the most important factor. Cooling rates of typical solidification processes, such as casting, centrifugal metallic mold casting, arc-melting, and single-roller melt spinning, are reported to be < 100 K/s [14], in the order of 100 K/s [15], approximately 2000 K/s [3], and 10^5 K/s [16], respectively. In contrast, the cooling rate in SLM process has been estimated to be 10^5 – 10^7 K/s [17,18]. We hypothesized that this ultrahigh cooling rate during SLM prevents extensive elemental segregation, leading to high-performance BioHEA parts. However, AM fabrication of TiNbTaZrMo BioHEA has not yet been attempted due to the difficulty of fabricating pre-alloyed powders with a targeted composition. The constituent elements in BioHEAs developed to date were similar to those in refractory HEAs (RHEAs) [19], as producing pre-alloyed powders was extremely difficult because of the high melting temperatures of the constituent elements.

Here, we report the production of BioHEA parts via the SLM method using pre-alloyed BioHEA powders. Furthermore, the formation of characteristic solidification microstructures in BioHEA products through the segregation suppression during solidification, and the simultaneous achievement of superior mechanical properties and biocompatibility are discussed. We demonstrate the potential of additively manufactured BioHEA for biomedical applications.

The $\text{Ti}_{1.4}\text{Nb}_{0.6}\text{Ta}_{0.6}\text{Zr}_{1.4}\text{Mo}_{0.6}$ BioHEA, which was modified from equiatomic TiNbTaZrMo to reduce the melting point and improve the room-temperature ductility [4], was used. The empirical alloy parameters [20,21] of mixing entropy, mixing enthalpy, difference in atomic radii, Ω -parameter, and average valence electron concentration in $\text{Ti}_{1.4}\text{Nb}_{0.6}\text{Ta}_{0.6}\text{Zr}_{1.4}\text{Mo}_{0.6}$ were 1.52R, where R is the gas constant, -0.75 kJ/mol, 6.15, 38.0, and 4.52, respectively. The alloy parameters indicate a high solid solution formation tendency with a body-centered cubic (BCC) structure in $\text{Ti}_{1.4}\text{Nb}_{0.6}\text{Ta}_{0.6}\text{Zr}_{1.4}\text{Mo}_{0.6}$ BioHEA. The distribution coefficients of each element at the liquidus temperature estimated by thermodynamic calculations using FactSage and SGTE2017 were 0.72, 1.18, 1.54, 0.80, and 1.41 for Ti, Nb, Ta, Zr, and Mo, respectively, which deviate significantly from 1 and indicate a strong tendency for two-phase separation via segregation, as reported previously [4].

$\text{Ti}_{1.4}\text{Nb}_{0.6}\text{Ta}_{0.6}\text{Zr}_{1.4}\text{Mo}_{0.6}$ BioHEA spherical powders were obtained by electrode induction melting gas atomization of pre-alloyed rods (Fig. 1(a)). Details of the applied process will be published separately. The as-obtained powders were conditioned by sieving to 10–63 μm (D50: 26.8 μm).

Products with dimensions of 5 mm (depth) \times 5 mm (length) \times <10 mm (height) were manufactured in an Ar atmosphere using an SLM apparatus (EOS M290, EOS, Germany) with a laser power, scanning speed, hatch distance, and layer thickness of 360 W, 1200 mm/s, 80 μm , and 60 μm , respectively. Here, the build direction was defined as the z-direction, and the two laser scanning directions were the x- and y-directions. To demonstrate the shape customizability, we also attempted to fabricate a jungle gym-structured BioHEA with a side of 10 mm and a beam width of 0.7 mm. The specimen's constituent phases, microstructure, composition distribution, and crystallographic orientation distribution were investigated by X-ray diffraction (XRD) (X'Pert PRO, PANalytical, Netherlands), energy dispersive X-ray spectroscopy (EDS) (Astec 3.1, Oxford Instruments, UK), and electron backscatter diffraction (EBSD) (NordlysMax³, Oxford Instruments, UK) with field-emission scanning electron microscopy (FE-SEM) (JIB-4610F, JEOL, Japan). To evaluate the mechanical properties, rectangular specimens with dimensions of approximately 2 mm \times 2 mm \times 5 mm were cut

from the products. Compression tests ($n = 3$) were conducted using an Instron-type testing machine (AG-X, Shimadzu, Japan) at a nominal strain rate of $1.67 \times 10^{-4} \text{ s}^{-1}$ at room temperature. A non-contact extensometer (TRViewX, Shimadzu, Japan) was used to detect the strain for the determination of Young's modulus. To evaluate biocompatibility, the cell culture experiment was performed according to a previously described protocol [6]. The specimens were cut into plates of 5 mm \times 5 mm \times 1 mm. The plate specimens of commercially pure Ti (CP-Ti), 316L-type stainless steel (SS316L), and arc-melted $\text{Ti}_{1.4}\text{Nb}_{0.6}\text{Ta}_{0.6}\text{Zr}_{1.4}\text{Mo}_{0.6}$ alloy (as-cast) [4] were prepared as reference materials ($n = 4$ –5). Primary osteoblasts were isolated from neonatal mice calvariae, diluted to 8000 cells/cm², and cultured on the specimens for 24 h in a 5% CO₂ humidified atmosphere. Cell density was evaluated using Giemsa staining (FUJIFILM Wako Chemicals, Japan). Moreover, immunocytochemistry was evaluated [6]. The quantitative results are expressed as the mean \pm standard deviation. Statistical significance was assessed using a one-way analysis of variance followed by Tukey's posthoc test. A *P*-value < 0.05 was considered statistically significant.

Fig. 1(a) shows the appearance and XRD pattern of the powders. The XRD pattern indicated the BCC solid solution with a peak split. SEM and EDS investigations represented a pore-free dendrite-type microstructure (Supplementary Fig. 1S). While the dendrite phase (purple) was rich in Nb, Ta, and Mo compared with the overall composition, the inter-dendrite phase (green) was rich in Ti and Zr.

Dense products with a porosity of less than 0.5% were obtained (Fig. 1(b)). The top surface of the product was overall flat. There was no lack of fusion type pores; therefore, the laser energy used for fabrication was appropriate for this alloy. The XRD peaks of the product were indexed as BCC structure (Fig. 1(b)). It should be emphasized that the peak separation was reduced, indicating a solid BCC solution with suppressed elemental segregation. No peaks corresponding to intermetallic compounds and/or BCC-based ordering structures were observed. Moreover, a jungle gym shape without any cracks and deformation or beam fragmentation was successfully achieved via SLM (Fig. 1(c)).

The SLM-built $\text{Ti}_{1.4}\text{Nb}_{0.6}\text{Ta}_{0.6}\text{Zr}_{1.4}\text{Mo}_{0.6}$ BioHEA product exhibited a unique solidification microstructure, as shown in Fig. 2. One of the remarkable features was the formation of a fine grain structure with the segregation suppression and a bimodal grain size distribution. Inverse pole figure (IPF) maps at low magnification taken in the xy-plane (Fig. 2(a1, a2)) demonstrated a stripe-like pattern with a relatively coarse grain region and a very fine grain region. From the IPF map in the yz-plane (Fig. 2(a3, a4)), it could be recognized that fine grains were equiaxed and present along the melt pool edge. In the yz-plane, the melt pool transverse cross-section formed by the X-scan with semi-elliptical shape and the longitudinal melt pool cross-section formed by the Y-scan running horizontally were stacked alternately along the z-direction. In the relatively coarse grain region, the grains elongated vertically in the melt pool longitudinal cross-section and elongated radially toward the melt pool center in the transverse cross section. The overall crystallographic texture can be described as a fiber texture where {100} preferentially orients in the z-direction (Fig. 2(a5)).

To analyze the microstructure of fine grain region which is a characteristic of this material, observations at high magnification were conducted. From the backscattered electron (BSE) image (Fig. 2(b1)), fine grains were observed at the bottom of the melt pool. The average fine grain size was 0.25 μm based on the high-angle grain boundary (Fig. 2(b3)). The crystallographic texture of the fine grain region was almost random. Immediately beneath the fine grain region, there were elongated grains with {100} orients in the z-direction. The average dimensions of the elongated grains were 2.5 μm and 31 μm in width and length, respectively.

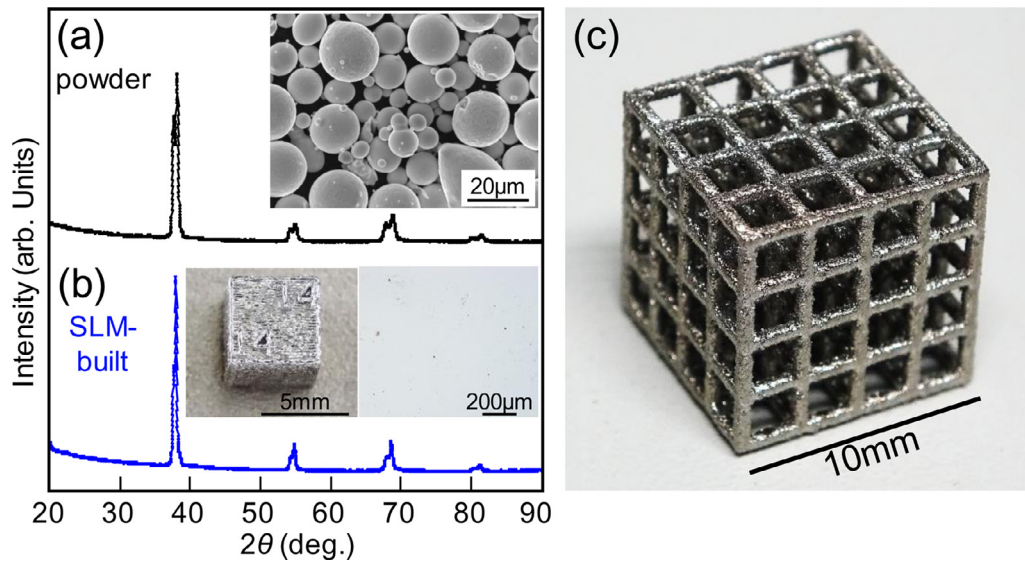


Fig. 1. Powder and SLM-built $\text{Ti}_{1.4}\text{Nb}_{0.6}\text{Ta}_{0.6}\text{Zr}_{1.4}\text{Mo}_{0.6}$ BioHEA, and their XRD patterns. (a) SEM image and XRD pattern of gas-atomized powder, (b) appearance and cross-sectional optical microscope image, and XRD pattern of SLM-built cube specimen, and (c) appearance of SLM-built jungle gym-shaped product.

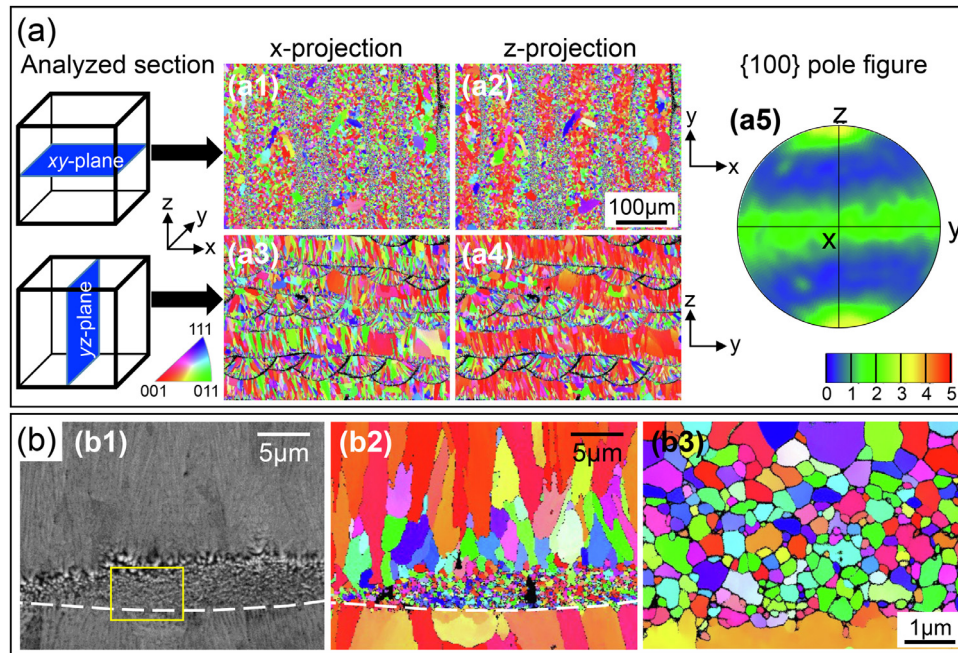


Fig. 2. Microstructural and crystallographic analyses of SLM-built $\text{Ti}_{1.4}\text{Nb}_{0.6}\text{Ta}_{0.6}\text{Zr}_{1.4}\text{Mo}_{0.6}$ BioHEA specimen. (a) IPF maps taken in the xy- and yz-planes, and pole figure representing a fiber texture in which {100} preferentially orients in z-direction. The black line that is seen in the IPF maps indicates not the crack but the part where the Kikuchi line could not be analyzed in EBSD analysis at low magnification. The very fine grains shown in (b3) are present in this portion. (b) BSE image and the corresponding IPF map, and magnified IPF map in the squared part in (b1). The very fine grains with random crystallographic orientation are present at the melt pool bottom and relatively large elongated grains occupies other regions in the melt pool, resulting in characteristic bimodal microstructure.

The length was much shorter than the 60-μm layer thickness. The interface (broken lines in Fig. 2(b1, b2)) between the fine equiaxed grain region and the underlying elongated grain region corresponded to the melt pool boundary and was smooth, and no crystallographic orientation continuity was present (Fig. 2(b2, b3)). The microstructure conformation inside a melt pool (fine equiaxed grains on the bottom and elongated grains in the center of the melt pool) is opposite to what is explained based on the conventional solidification theory [22,23], in which the balance between the thermal gradient (G) and the migration velocity of the solid/liquid interface (R) determines the microstructure type.

At the melt pool bottom, a higher G/R is observed due to the large G and small R . As the solidification progresses toward the center of the melt pool, G decreases and R increases; thus, G/R decreases [24,25]. As a result, equiaxed grains normally appear in the melt pool center with low G/R [18]. The equiaxed grains are eventually re-melted by the melting of the next layer, enabling epitaxial growth at the melt pool boundary. In contrast, equiaxed grains without preferential orientation at the bottom of the melt pool observed in this study hindered epitaxial crystal growth along the z-direction. The bimodal solidification structure could not be effectively explained only by the consideration of G/R . The possible

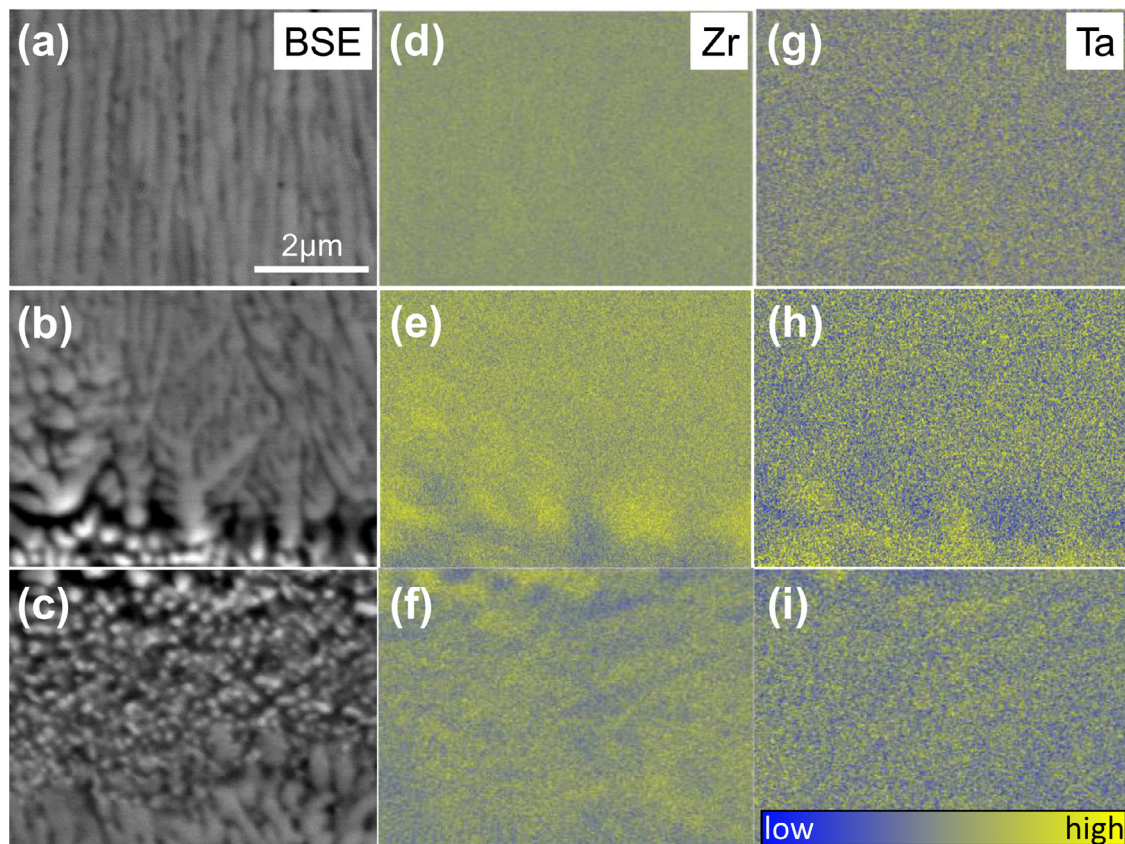


Fig. 3. Compositional distribution analyses of SLM-built $\text{Ti}_{1.4}\text{Nb}_{0.6}\text{Ta}_{0.6}\text{Zr}_{1.4}\text{Mo}_{0.6}$ BioHEA specimen. (a–c) BSE images, (d–f) EDS maps for Zr, and (g–i) EDS maps for Ta. The difference in concentration was slight, indicating that the elemental segregation was considerably suppressed via SLM. The EDS images are displayed with high contrast for the visibility of a slight difference in concentration.

mechanism for the formation of this unique bimodal structure is discussed below.

Fig. 3 shows the BSE images and EDS compositional distribution maps taken around the fine grain region to investigate the segregation tendency in the SLM products. As expected, elemental segregation was largely suppressed in the SLM-built specimen compared to the cast material prepared by arc melting (Supplementary Fig. S2). SLM-built specimens also showed dendritic solidification structures, but their size was quite small, and the composition distribution was almost uniform. In the SLM-built specimen, Ti and Zr tended to be slightly enriched in the inter-dendrite region, and Nb, Ta, and Mo in the dendrite region; this is a similar tendency to that in the cast material (Supplementary Fig. S2) [4] and the powder (Supplementary Fig. S1). The EDS quantitative data (Supplementary Table S1) clearly indicated that, as expected, the SLM process effectively suppressed elemental segregation and realized a super-solid solution owing to ultrahigh cooling rate.

The fine dendrite structure formation in the SLM process resulted from the increased nucleation frequency at the bottom of the melt pool. Under high temperature by laser irradiation, the previously solidified part is re-melted, and the dendrite tip can be detached and then transported into the melt, acting as a favorable nucleation site [26]. This is one possible condition for the fine grain formation at the bottom of the melt pool.

The epitaxial growth at the melt pool boundary plays a crucial role in crystallographic texture formation. The implementation of epitaxial growth can result in a highly textured microstructure [27–30]. By applying scan strategy XY to metallic materials with cubic crystal structures in which $\langle 100 \rangle$ is an easy growth direction [31], a cube texture where $\{100\}$ is aligned in the x-, y-, and

z-directions is obtained [32–35]. Once the cube texture is stabilized, it is easy to inherit a crystallographic orientation of both X- and Y-scans through epitaxial growth. Therefore, grain boundaries with a large angle difference are culled, and a single crystalline-like structure is obtained. Namely, the decrease in grain boundary energy becomes the driving force for stabilizing the cube texture. In this study, the formation of fine grains became an obstacle to epitaxial growth. Only the grains with $\{100\}$ approximately parallel to the heat flow direction selectively survived and grew in the heat flow direction (z-direction), resulting in the fiber texture evolution with $\{100\}$ orientation in the z-direction.

The SLM-built $\text{Ti}_{1.4}\text{Nb}_{0.6}\text{Ta}_{0.6}\text{Zr}_{1.4}\text{Mo}_{0.6}$ BioHEA showed excellent mechanical properties. The typical true stress-true plastic strain curve of the specimen is shown in Supplementary Fig. S3. The 0.2% proof stress reached 1690 ± 78 MPa, which is significantly higher than that of cast $\text{Ti}_{1.4}\text{Nb}_{0.6}\text{Ta}_{0.6}\text{Zr}_{1.4}\text{Mo}_{0.6}$ (1140 MPa) [4]. True strain at break was $1.32 \pm 0.19\%$, indicating moderate room-temperature ductility. This remarkable increase in the proof stress should be due to the combined effect of grain boundary strengthening owing to grain refinement and enhanced solid solution strengthening [36] achieved by suppressing elemental segregation and thus realizing super-solid solution. These benefits are drawn by the rapid SLM cooling rates. The Young's modulus was measured to be 140 ± 9 GPa, an intermediate value of frequently used metallic biomaterials, such as CP-Ti, Ti–6Al–4V (110 GPa), and SS316L (~200 GPa) [37]. We have succeeded in imparting excellent mechanical properties to a BioHEA as a metallic biomaterial using the rapid solidification feature that is unique to SLM.

Fig. 4 shows the biocompatibility of SLM-built $\text{Ti}_{1.4}\text{Nb}_{0.6}\text{Ta}_{0.6}\text{Zr}_{1.4}\text{Mo}_{0.6}$, together with as-cast counterparts,

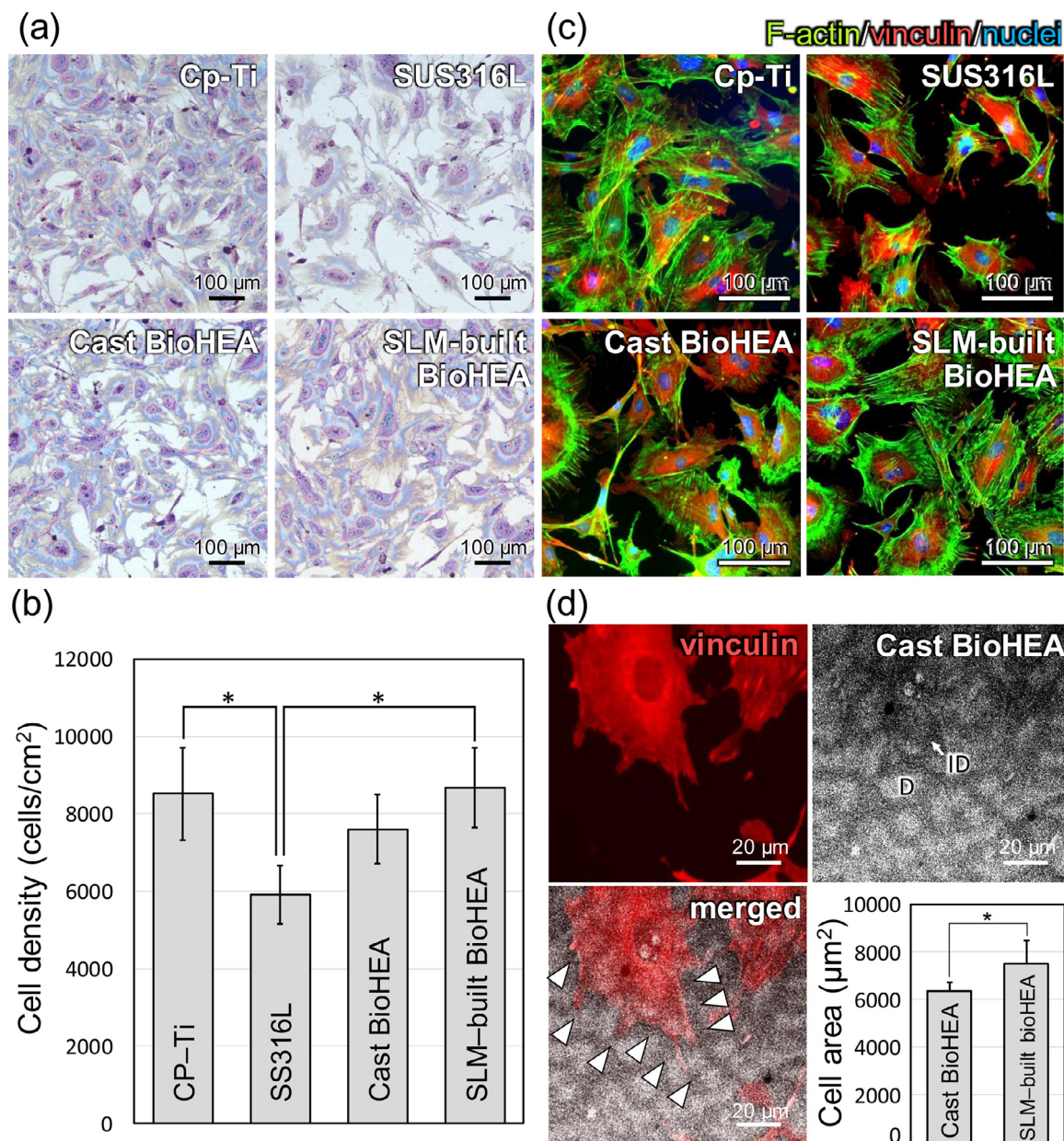


Fig. 4. Biocompatibility analysis of SLM-built $\text{Ti}_{1.4}\text{Nb}_{0.6}\text{Ta}_{0.6}\text{Zr}_{1.4}\text{Mo}_{0.6}$ BioHEA specimen. (a) Giemsa staining images of osteoblasts cultured on SLM-built specimen and reference materials of CP-Ti, SS316L, and cast BioHEA counterpart. (b) Quantitative analysis of cell density. *: $P < 0.05$. (c) Fluorescent images of osteoblast adhesion on SLM-built BioHEA, CP-Ti, SS316L, and cast BioHEA. (d) Localization of osteoblast adhesion spots on the cast BioHEA specimen with extensive elemental segregation and analyzed cell area for cast and SLM-built BioHEAs. On cast BioHEA, cell filopodia preferentially (rather restrictedly) locates on the inter-dendrite (ID) region with enriched Ti and Zr, resulting in inhibited cell spreading. *: $P < 0.05$.

CP-Ti, and SS316L. Fig. 4(b) shows the osteoblast density adhered to the specimens evaluated by Giemsa staining images (Fig. 4(a)). The cell density on the SLM-built specimen was comparable to that on the CP-Ti and cast counterpart, and was significantly higher than that on SS316L. Moreover, a cell morphology, which directly influences the following cellular events involving tissue or organ construction, provided characteristic properties among the alloys examined. Fig. 4(c) shows fluorescent images of cytoskeletal components and focal adhesions of osteoblasts adhered to the specimens. The osteoblasts on the SLM-built specimen showed a widespread morphology with a dense network of actin fibers, and those on CP-Ti and cast specimens. Moreover, the uniform distribution of the composition in SLM-built specimens exhibited distinct advantages for cell spreading, reflecting the cells' osteogenic ability [38]. The elemental segregation in cast material restricted

the filopodia distribution in osteoblasts by holding the adhesion spots in Ti- and Zr-enriched inter-dendrite regions, resulting in the reduced cell spreading area on cast material (Fig. 4(d)). Ti- and Zr-enrichment likely induced the extracellular matrix protein-satisfied microenvironment to develop cell adhesion molecules involving integrin. The SLM-built $\text{Ti}_{1.4}\text{Nb}_{0.6}\text{Ta}_{0.6}\text{Zr}_{1.4}\text{Mo}_{0.6}$ was found to be much more advantageous than SS316L for bone tissue compatibility, and the biocompatibility was comparable to that of CP-Ti, the most common metals used in biomedical applications.

In conclusion, the extremely high cooling rate in the SLM process effectively suppressed the elemental segregation even for the ultra-multi-component HEA system, which was not achieved via conventional solidification processes. The SLM-built specimens showed superior yield strength and comparable biocompatibility to cast counterparts with custom-made shape capability. The SLM-

built $\text{Ti}_{1.4}\text{Nb}_{0.6}\text{Ta}_{0.6}\text{Zr}_{1.4}\text{Mo}_{0.6}$ BioHEA is a promising near-future metallic biomaterial.

This work was supported by Grants-in-Aid for Scientific Research from the Japan Society for the Promotion of Science (JSPS) [grant number JP18H05254]. This work was also partly supported by the Cross-Ministerial Strategic Innovation Promotion Program (SIP) – Materials Integration for Revolutionary Design System of Structural Materials – Domain C1: “Development of Additive Manufacturing Process for Ni-based Alloy” from the Japan Science and Technology Agency (JST).

Declaration of Competing Interest

The authors declare that they have no known competing financial interests or personal relationships that could have appeared to influence the work reported in this paper.

Supplementary materials

Supplementary material associated with this article can be found, in the online version, at doi:[10.1016/j.scriptamat.2020.113658](https://doi.org/10.1016/j.scriptamat.2020.113658).

References

- [1] Y.J. Liu, S.J. Li, H.L. Wang, W.T. Hou, Y.L. Hao, R. Yang, T.B. Sercombe, L.C. Zhang, *Acta Mater.* 113 (2016) 56–67.
- [2] M. Todai, T. Nagase, T. Hori, A. Matsugaki, A. Sekita, T. Nakano, *Scr. Mater.* 129 (2017) 65–68.
- [3] T. Nagase, K. Mizuuchi, T. Nakano, *Entropy* 21 (2019) 483.
- [4] T. Hori, T. Nagase, M. Todai, A. Matsugaki, T. Nakano, *Scr. Mater.* 172 (2019) 83–87.
- [5] T. Nagase, M. Todai, T. Hori, T. Nakano, *J. Alloys Compd.* 753 (2018) 412–421.
- [6] T. Nagase, Y. Iijima, A. Matsugaki, K. Ameyama, T. Nakano, *Mater. Sci. Eng. C-107* (2020) 110322.
- [7] A. Motallebzadeh, N.S. Peighambari, S. Sheikh, H. Murakami, S. Guo, D. Canadinc, *Intermetallics* 113 (2019) 106572.
- [8] Y. Yuan, Y. Wu, Z. Yang, X. Liang, Z. Lei, H. Huang, H. Wang, X. Liu, K. An, W. Wu, Z. Lu, *Mater. Res. Lett.* 7 (2019) 225–231.
- [9] G. Popescu, B. Ghiban, C.A. Popescu, L. Rosu, R. Trusca, I. Carcea, V. Soare, D. Dumitrescu, I. Constantin, M.T. Olaru, B.A. Carlan, in: *Proceedings of the IOP 400 Conference Series*, 2018.
- [10] G. Perumal, H.S. Grewal, M. Pole, L.V.K. Reddy, S. Mukherjee, H. Singh, G. Manivasagam, H.S. Arora, *ACS Appl. Bio Mater.* 3 (2020) 1233–1244.
- [11] S.P. Wang, J. Xu, *Mater. Sci. Eng. C-73* (2017) 80–89.
- [12] Y. Qiu, S. Thomas, M.A. Gibson, H.L. Fraser, N. Birbilis, *npj Mater. Degrad.* 1 (2017) 15.
- [13] J.K. Jensen, B.A. Welk, R.E.A. Williams, J.M. Sosa, D.E. Huber, O.N. Senkov, G.B. Viswanathan, H.L. Fraser, *Scr. Mater.* 121 (2016) 1–4.
- [14] E. Lee, B. Mishra, *Mater. Trans.* 58 (2017) 1624–1627.
- [15] T. Nagase, M. Takemura, M. Matsumuro, T. Maruyama, *Mater. Trans.* 59 (2018) 255–264.
- [16] R.W. Cahn, *Physical Metallurgy*, third ed., Elsevier Science Publishers, North-Holland, 1996.
- [17] Q. Jia, P. Rometsch, P. Kürsteiner, Q. Chao, A. Huang, M. Weyland, L. Bourgeois, X. Wu, *Acta Mater.* 171 (2019) 108–118.
- [18] D. Gu, Q. Shi, K. Lin, L. Xi, *Addit. Manuf.* 22 (2018) 265–278.
- [19] O.N. Senkov, J.M. Scott, S.V. Senkova, D.B. Miracle, C.F. Woodward, *J. Alloys Compd.* 509 (2011) 6043–6048.
- [20] M.C. Gao, J.-W. Yeh, P.K. Liaw, Y. Zhang, *Fundamentals and Applications*, first ed., Springer, Switzerland, 2016.
- [21] B.S. Murty, J.-W. Yeh, S. Ranganathan, *High-Entropy Alloys*, first ed., Butterworth-Heinemann, Oxford, 2014.
- [22] F. Yan, W. Xiong, E.J. Faierman, *Materials* 10 (2017) 1260.
- [23] J.N. Dupont, *ASM Handbook, Volume 6A: Welding Fundamentals and Processes*, ASM International: Materials Park, OH, 2011.
- [24] K. Karayagiz, L. Johnson, R. Seede, V. Attari, B. Zhang, X. Huang, S. Ghosh, T. Duong, I. Karaman, A. Elwany, R. Arróyave, *Acta Mater.* 185 (2020) 320–339.
- [25] P. Promopattum, S.C. Yao, P.C. Pistorius, A.D. Rollett, *Engineering* 3 (2017) 685–694.
- [26] R. Shi, S.A. Khairallah, T.T. Roehling, T.W. Heo, J.T. McKeown, M.J. Matthews, *Acta Mater.* 184 (2020) 284–305.
- [27] M.S. Pham, B. Dovgii, P.A. Hooper, C.M. Gourlay, A. Piglion, *Nat. Commun.* 11 (2020) 749.
- [28] T. Ishimoto, S. Wu, Y. Ito, S.H. Sun, H. Amano, T. Nakano, *ISIJ Int.* 60 (2020) 1758–1764.
- [29] S.H. Sun, T. Ishimoto, K. Hagihara, Y. Tsutsumi, T. Hanawa, T. Nakano, *Scr. Mater.* 159 (2019) 89–93.
- [30] N. Nadammal, S. Cabeza, T. Mishurova, T. Thiede, A. Kromm, C. Seyfert, L. Farahbod, C. Haberland, J.A. Schneider, P.D. Portella, G. Bruno, *Mater. Des.* 134 (2017) 139–150.
- [31] R.W. Messler, *Principles of Welding*, Wiley, NY, 2008.
- [32] O. Gokcekaya, N. Hayashi, T. Ishimoto, K. Ueda, T. Narushima, T. Nakano, *Addit. Manuf.* (2020) 101624.
- [33] J. Zou, Y. Gaber, G. Voulazeris, S. Li, L. Vazquez, L.-F. Liu, M.-Y. Yao, Y.-J. Wang, M. Holynski, K. Bongs, M.M. Attallah, *Acta Mater.* 158 (2018) 230–238.
- [34] T. Ishimoto, K. Hagihara, K. Hisamoto, S.H. Sun, T. Nakano, *Scr. Mater.* 132 (2017) 34–38.
- [35] F. Geiger, K. Kunze, T. Etter, *Mater. Sci. Eng. A* 661 (2016) 240–246.
- [36] J.W. Yeh, *JOM* 65 (2013) 1759–1771.
- [37] M. Niinomi, *Sci. Technol. Adv. Mater.* 4 (2003) 445–454.
- [38] Y. Yang, X. Wang, Y. Wang, X. Hu, N. Kawazoe, Y. Yang, G. Chen, *Sci. Rep.* 9 (2019) 6891.